Check for updates

Small

NANO · MICRO small
www.small-journal.com

RESEARCH ARTICLE OPEN ACCESS

Hydrogen Bonding Denticity Governs Surface Modulation in Inorganic Perovskite Nanocrystals

Jiaxin Song[1] | Gyeong Eun Seok[1] | Junsu Son[2,3] | Woo Hyeon Jeong[1] | Dong Gyu Lee[2,3] | Sung Woo Jang[4] | Xinyu Shen[5] | Gayoung Seo[6] | Zhongkai Yu[7] | Dongyeong Gim[8] | Jongmin Choi[6] | Won Bin Im[4] | Tae Kyung Lee[2,3] | Minjeong Ha[8] | Bo Ram Lee[1]

[1]School of Advanced Materials Science and Engineering, Sungkyunkwan University, Suwon, Gyeonggi-do, Republic of Korea | [2]Department of Organic and Nano Engineering, Hanyang University, Seoul, Republic of Korea | [3]Human-Tech Convergence Program, Hanyang University, Seoul, Republic of Korea | [4]Division of Materials Science and Engineering, Hanyang University, Seoul, Republic of Korea | [5]Clarendon Laboratory, Department of Physics, University of Oxford, Oxford, UK | [6]Department of Energy Science and Engineering, Daegu Gyeongbuk Institute of Science and Technology (DGIST), Daegu, Republic of Korea | [7]School of Physics and Optoelectronic Engineering, Yangtze University, Jingzhou, China | [8]School of Materials Science and Engineering, Gwangju Institute of Science and Technology (GIST), Gwangju, Republic of Korea

Correspondence: Tae Kyung Lee (tklee@hanyang.ac.kr) | Minjeong Ha (minjeongha@gist.ac.kr) | Bo Ram Lee (brlee@skku.edu)

Received: 11 May 2026 | **Revised:** 21 August 2026 | **Accepted:** 26 August 2026

Keywords: hydrogen bonding | perovskite nanocrystals | perovskite light-emitting diodes | surface modulation | surface passivation

ABSTRACT

All-inorganic $CsPbI_3$ perovskite nanocrystals (PNCs) have emerged as promising emitters for optoelectronic applications owing to their high color purity, tunable bandgap, and high photoluminescence quantum yield (PLQY). However, dynamic surface ligands, abundant trap states, and rapid halide ion migration limit their emission efficiency and operational stability. Here, methylammonium (MA^+), formamidinium (FA^+), and guanidinium (GA^+) were systematically investigated as surface modulators for PNCs via an anti-solvent-assisted post-treatment strategy. Spectroscopic analyses and density functional theory calculations reveal that the passivation efficacy is determined by the strength and denticity of hydrogen-bonding interactions between the organic cations and the PNC surface. Among the three candidates, GA^+ exhibits the highest efficacy owing to its trifunctional N—H groups, which enable robust multidentate surface interactions that suppress trap formation and halide ion migration. As a result, GA-treated PNCs achieve a PLQY of 99.3% and retain ~80% of their initial PLQY after 9 days under ambient conditions. The resulting perovskite light-emitting diodes deliver a maximum external quantum efficiency of 10.2% and a maximum luminance of 473 cd m^{-2}, representing a significant improvement over pristine devices. These findings identify molecular hydrogen-bonding geometry as a key design parameter for surface engineering of efficient and stable PNC-based optoelectronic devices.

1 | Introduction

Metal halide perovskite nanocrystals (PNCs) have attracted significant attention over the past decade for optoelectronic applications such as solar cells, light-emitting diodes, and photodetectors [1–5]. In particular, PNCs have been regarded as promising materials for next-generation displays because of their exceptional defect tolerance, high color purity, facile bandgap tunability, and near-unity photoluminescence quantum yield (PLQY) [6–13]. Despite these outstanding optoelectronic merits, the dynamic and weakly coordinated surface ligands of PNCs are readily detached during purification, film formation, and

Jiaxin Song, Gyeong Eun Seok, and Junsu Son contributed equally to this work.

This is an open access article under the terms of the Creative Commons Attribution License, which permits use, distribution and reproduction in any medium, provided the original work is properly cited.
© 2026 The Author(s). *Small* published by Wiley-VCH GmbH

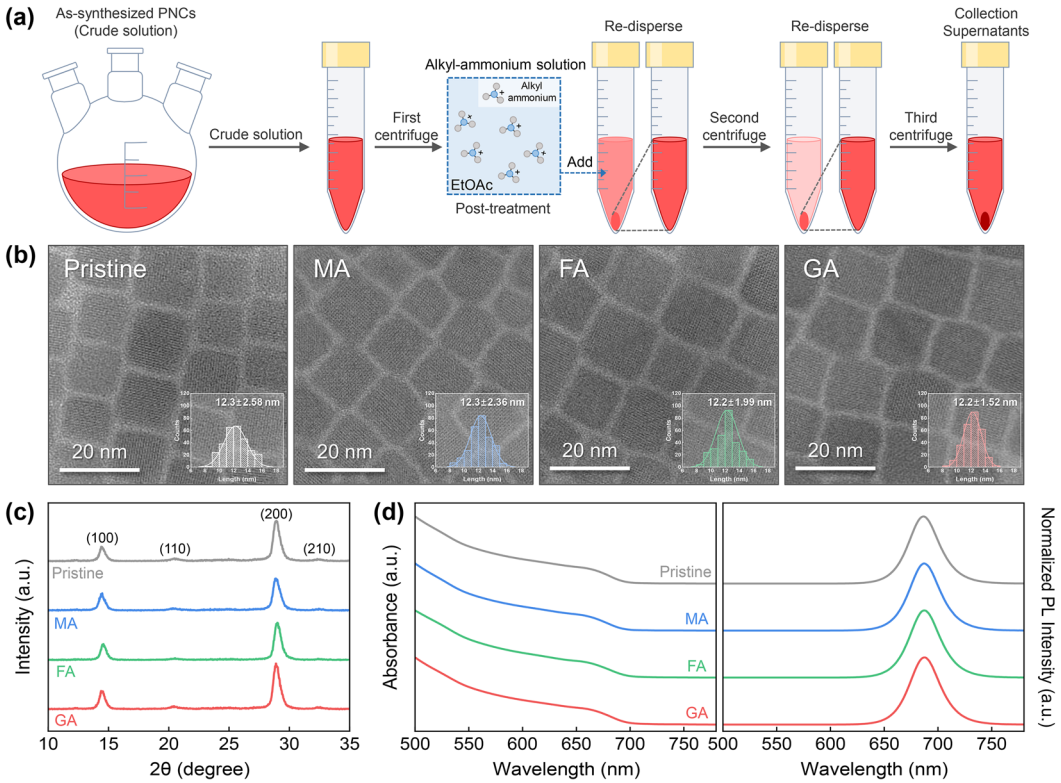

FIGURE 1 | Structural and optical characterization of pristine, MA-, FA-, and GA-treated PNCs. (a) Schematic illustration of the anti-solvent-assisted surface modulation strategy. (b) TEM images with inset size distribution histograms, (c) XRD patterns, (d) UV–vis absorption and normalized PL spectra of each sample.

device operation, creating undercoordinated surface sites and abundant trap states that promote non-radiative recombination [14–17]. More critically, these surface traps act synergistically with accelerated ion migration to drive rapid phase instability, which imposes severe limitations on the operational lifetime of perovskite light-emitting diodes (PeLEDs) [18, 19].

To address these challenges, surface passivation has emerged as a key strategy for improving both the optoelectronic properties and operational stability of PNCs [20–22]. Various approaches, including ligand engineering, divalent metal ion doping, and organic ammonium halide passivation, have been developed to reduce surface trap densities and suppress ion migration [17, 23–27]. Among these, organic ammonium halides have been widely adopted as a simple yet effective passivation strategy because they simultaneously compensate halide vacancies and coordinate undercoordinated surface sites [28–30]. Diverse cations, including methylammonium (MA^+), formamidinium (FA^+), and guanidinium (GA^+), have been investigated as surface passivating agents for PNCs. These additives are typically introduced either during synthesis or through post-synthetic treatment. Incorporation during synthesis often results in partial lattice substitution or bulk modification, which can perturb the crystal structure and alter the emission characteristics of PNCs [18, 21, 29, 31, 32]. In contrast, post-synthetic treatment enables selective surface passivation while largely preserving the structural integrity of the perovskite core, and has therefore attracted particular attention as an effective route toward high-quality PNC emitters for efficient and stable PeLEDs [33–38].

Despite these advances, a systematic understanding of how the chemical structure of organic ammonium halides governs surface defect passivation, interfacial interactions, and the resulting optoelectronic properties of all-inorganic $CsPbI_3$ PNCs remains elusive. Although MA, FA, and GA cations share closely related molecular backbones with a systematically increasing number of N—H groups, a direct comparative study correlating their surface interaction mechanisms with hydrogen-bonding denticity has not been established. Such a comparison is essential for elucidating clear structure-property relationships and providing a rational foundation for the design of high-performance surface modulators.

Herein, we present a systematic comparative investigation of MA, FA, and GA cations as surface modulators for all-inorganic $CsPbI_3$ PNCs, and identify hydrogen-bonding denticity as a key molecular descriptor of their surface-modulation efficacy, with GA^+ exhibiting the strongest surface interaction owing to its multiple N—H hydrogen-bond donors. As a result, GA-treated PNCs achieve a PLQY of 99.3%, compared with 78.5% for pristine PNCs, together with substantially improved long-term photoluminescence (PL) stability. Notably, GA-treated PNCs retain ~80% of their initial PLQY after 9 days at 22.5°C and 15% relative humidity (RH), whereas pristine PNCs decline to ~40% over the same period. PeLEDs based on this strategy exhibit a maximum external quantum efficiency (EQE) of 10.2% and a maximum luminance of 473 cd m^{-2}, significantly outperforming pristine devices (7.2% EQE and 231 cd m^{-2}). This work identifies hydrogen-bonding denticity as a key factor governing surface

16136829, 2026, 64, Downloaded from https://onlinelibrary.wiley.com/doi/10.1002/smll.75614 by Hanyang University Library, Wiley Online Library on [22/11/2026]. See the Terms and Conditions (https://onlinelibrary.wiley.com/terms-and-conditions) on Wiley Online Library for rules of use; OA articles are governed by the applicable Creative Commons License

modulation in PNCs and provides a rational basis for the design of efficient and stable perovskite optoelectronic devices.

2 | Results and Discussion

2.1 | Structural and Optical Characterization of Surface-Treated $CsPbI_3$ PNCs

Pristine $CsPbI_3$ PNCs were synthesized via a conventional hot-injection method [39]. To modify the PNC surface without inducing structural damage, an anti-solvent-assisted surface modulation strategy was adopted (Figure 1a) [15, 40, 41]. Specifically, organic modulators, namely MA, FA, and GA, dissolved in ethyl acetate (EtOAc), were introduced into the as-synthesized PNC dispersion, followed by purification. This post-treatment approach enables preferential surface anchoring of the modulators while minimizing unwanted cation incorporation into the bulk lattice, thereby preserving the structural integrity of the PNCs [40, 41].

To evaluate the impact of surface modulation on the physical properties of the PNCs, morphological and structural analyses were first performed. TEM images reveal that all samples retain a well-defined cubic morphology with negligible variations in average crystal sizes of 12.3 ± 2.6 nm (pristine), 12.3 ± 2.4 nm (MA), 12.2 ± 2.0 nm (FA), and 12.2 ± 1.5 nm (GA) (Figure 1b and Figure S1). These results confirm that the surface modulation is non-destructive and does not induce noticeable surface etching or aggregation.

XRD patterns were obtained to examine structural changes following surface modulation (Figure 1c). All samples retained the α-phase $CsPbI_3$ structure after surface modulation. Distinct diffraction peaks at $2\theta \approx 14.8°$, 20.8°, 29.4°, and 31.4° corresponding to the (100), (110), (200), and (210) crystal planes of α-$CsPbI_3$, remain unchanged after surface modulation [42]. The absence of peak shifts or impurity phases, including the non-photoactive δ-phase, suggests that the organic modulators are selectively anchored to the surface rather than being incorporated into Cs^+ sites within the bulk lattice [43, 44].

Consistent with the structural findings, the optical properties of the PNCs remained largely unchanged under optimized modulation conditions (Figure 1d). The absorption profiles and PL spectra exhibited no significant peak shifts, indicating that the intrinsic bandgap of $CsPbI_3$ was preserved. However, this structural preservation was strongly concentration-dependent. As shown in Figure S2, modulator concentrations above the optimum led to noticeable red-shifts in PL emission, suggesting partial cation incorporation into the bulk lattice or concentration-induced lattice strain. Consistently, devices based on PNCs treated above the optimal concentration exhibited inferior performance (Figure S3 and Table S1), indicating that the beneficial effects of the surface modulators are limited to an optimal treatment window. By contrast, at the optimized conctration, the absence of a noticeable PL shift is consistent with predominantly surface-localized modulation rather than substantial incorporation into the PNC lattice.

2.2 | Surface Chemistry and Modulation Mechanisms in Surface-Treated $CsPbI_3$ PNCs

To elucidate the surface chemistry underlying the observed structural preservation, XPS was performed. The Pb 4f spectra (Figure 2a) exhibit characteristic doublets for all samples, with Pb $4f_{5/2}$ and Pb $4f_{7/2}$ peaks located at 142.8 and 137.9 eV, respectively, for pristine PNCs. Upon surface modulation, both peaks progressively shift toward higher binding energies in the order of pristine, MA, FA, and GA, reaching 142.95 and 138.05 eV for the GA-treated sample. A similar trend is observed in the I 3d spectra (Figure 2b). These positive shifts are consistent with hydrogen-bonding interactions between the ammonium groups and surface iodides, which withdraw electron density from the Pb–I framework and induce an electronic deshielding effect. As the number of available N—H groups increases from MA to FA to GA, the magnitude of the shift becomes more pronounced, supporting progressively stronger multidentate surface interactions. To further verify the role of N—H-mediated interactions, tetramethylammonium iodide (TMAI), a quaternary ammonium salt lacking N—H hydrogen-bond donors, was examined as a control. TMAI-treated PNCs exhibited negligible changes in the Pb 4f and I 3d binding energies compared with pristine PNCs (Figure S4), further supporting that the observed surface electronic modulation is associated with N—H-mediated interactions rather than simply the presence of an ammonium cation. Additional insight is provided by the N 1s spectra (Figure S5). While all treated samples exhibit a dominant protonated ammonium peak at ~402 eV, an additional feature near ~400 eV, assigned to neutral amino groups, becomes increasingly pronounced after surface modulation. This peak is most intense in the GA-treated sample, consistent with the trifunctional structure of GA^+, whose multiple N—H groups enable more extensive and rigid hydrogen-bonding interactions with surface halides.

To further verify the presence of surface-anchored organic modulators, FT-IR spectroscopy was performed on pristine, MA-, FA-, and GA-treated PNC films (Figure 2c and Figure S6) [33, 34]. Vibrational bands at 2922 and 2851 cm^{-1}, corresponding to the C—H stretching modes of OLA and OAc ligands, are observed in all samples, confirming the retention of native surface ligands after treatment. Upon GA modulation, additional characteristic bands emerge. The symmetric and asymmetric N—H stretching modes at 3416 and 3337 cm^{-1}, respectively, together with the C═N stretching mode at 1532 cm^{-1}, are observed exclusively in the GA-treated sample, confirming successful anchoring of GA^+ on the PNC surface [33, 45]. These bands correspond well to the characteristic vibration modes of the GA^+. Notably, comparison with free GAI reveals pronounced broadening of the N—H stretching region in the GA-treated PNC films, indicating a substantially altered hydrogen-bonding environment upon surface binding (Figure S6). Together with the retention of the characteristic C═N vibration and the XPS results, these spectroscopic changes support hydrogen-bonding-mediated surface anchoring of GA^+ and its ability to establish multidentate interactions with surface halides.

To further elucidate the atomistic origin of surface stabilization and its effect on defect passivation, DFT calculations were performed. Surface defects are major sources of deep trap states

16136829, 2026, 64, Downloaded from https://onlinelibrary.wiley.com/doi/10.1002/smll.75614 by Hanyang University Library, Wiley Online Library on [22/11/2026]. See the Terms and Conditions (https://onlinelibrary.wiley.com/terms-and-conditions) on Wiley Online Library for rules of use; OA articles are governed by the applicable Creative Commons License

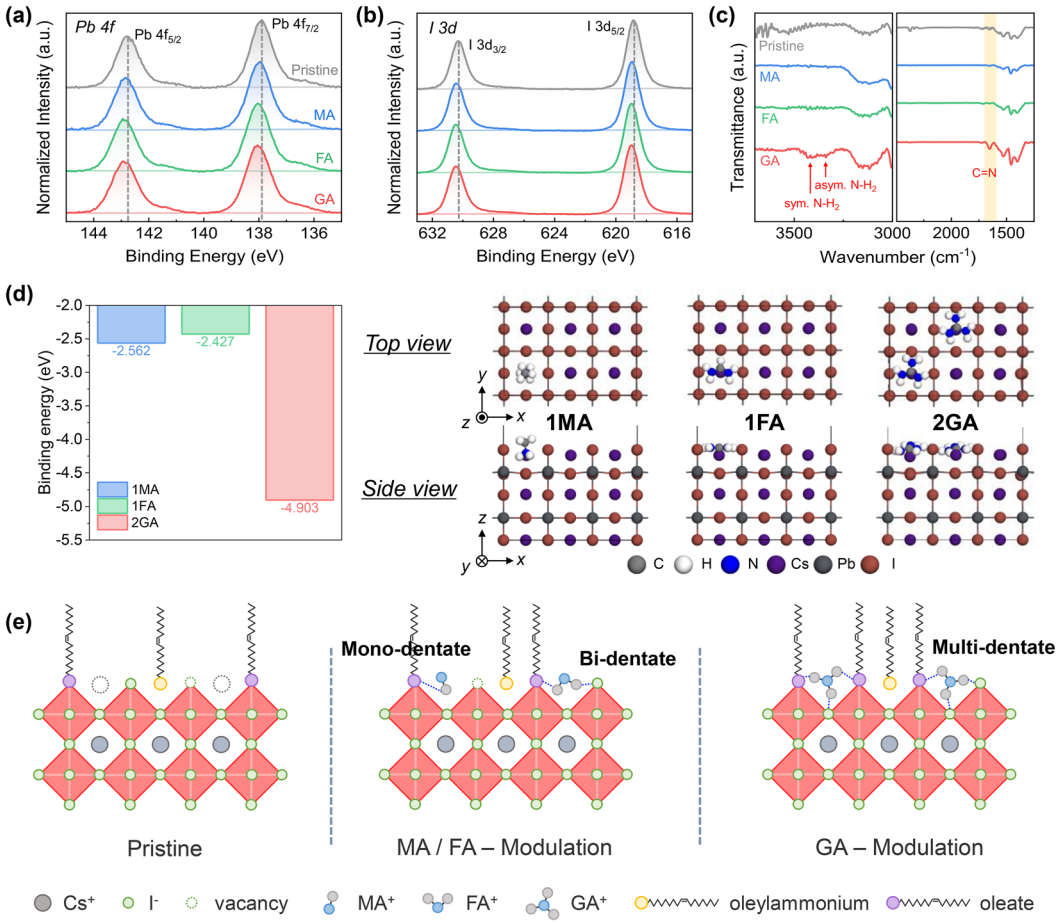

FIGURE 2 | Surface chemistry and modulation mechanisms of pristine, MA-, FA-, and GA-treated PNCs. (a) Pb 4f XPS spectra, (b) I 3d XPS spectra, (c) FT-IR spectra of each sample. (d) Binding energies of MA, FA, and two GA molecules on the surface of $CsPbI_3$ in the 1Top, 1Top, and 2Top configurations, respectively. (e) Schematic diagrams of the surface modulation mechanism in PNCs.

in halide perovskites; therefore, effective stabilization of the outermost surface is critical for minimizing defect-induced trap formation [46]. The normalized incorporation energies of $CsPbI_3$ surface models containing one, two, and three MA, FA, and GA molecules were calculated for the corresponding Top, Sub, and Top-Sub configurations (Figures S7 and S17). For each organic iodide species, the Top configurations (*i.e.*, 1Top, 2Top, and 3Top) were found to be the most energetically favorable, indicating that surface-layer incorporation was thermodynamically preferred over subsurface incorporation (Figure S18). Among the surface-incorporated systems, MA and FA exhibited their most favorable normalized incorporation energies in the 1Top configuration, whereas GA exhibited its most favorable incorporation energy in the 2Top configuration (Figure S19). The energetic preference for the 2Top configuration indicates that incorporation of two GA molecules can be favorably accommodated within the present surface model, consistent with the strong interfacial stabilization of GA on the $CsPbI_3$ surface. Consistent with the results shown in Figure S18, Boltzmann population analysis based on the calculated normalized incorporation energies revealed that MA, FA, and 2GA systems all preferentially adopted the Top configurations over the corresponding Sub-containing configurations (Figure S20). Notably, among the fully Top to fully Sub comparisons, the 2GA system exhibited the highest Top-to-Sub Boltzmann population ratio, indicating the strongest thermodynamic preference for surface localization and passivation of defect-sensitive surface sites. This preference was further supported by the stronger total interfacial binding of GA to the $CsPbI_3$ surface (Figure 2d and Figure S21). Although the relative binding energy of FA is higher than that of MA in the vacancy-filling surface model shown in Figure 2d, this result does not fully represent the overall surface incorporation behavior. Under realistic surface conditions, all three organic modulators can be incorporated at the surface through multiple pathways, including direct vacancy occupation, cation exchange with pre-existing Cs^+ ions, and local surface reconstruction. Therefore, the energetics presented in Figure 2d mainly represent one vacancy-passivation pathway, whereas the overall surface incorporation behavior is likely governed by the combined contributions of vacancy filling, cation exchange, and structural relaxation. Vacancy-filling energetics alone cannot fully describe the observed incorporation behavior. Moreover, GA incorporation increased the iodine-vacancy formation energy relative to the pristine surface, indicating reduced thermodynamic favorability of halide vacancy formation and enhanced surface defect suppression (Figure S22–S24).

The distinct passivation behaviors of the three organic modulators are further illustrated in the schematic diagram (Figure 2e). The trifunctional structure of GA^+ enables the formation of a dense multidentate hydrogen-bonding network with surface

16136829, 2026, 64, Downloaded from https://onlinelibrary.wiley.com/doi/10.1002/smll.75614 by Hanyang University Library, Wiley Online Library on [22/11/2026]. See the Terms and Conditions (https://onlinelibrary.wiley.com/terms-and-conditions) on Wiley Online Library for rules of use; OA articles are governed by the applicable Creative Commons License

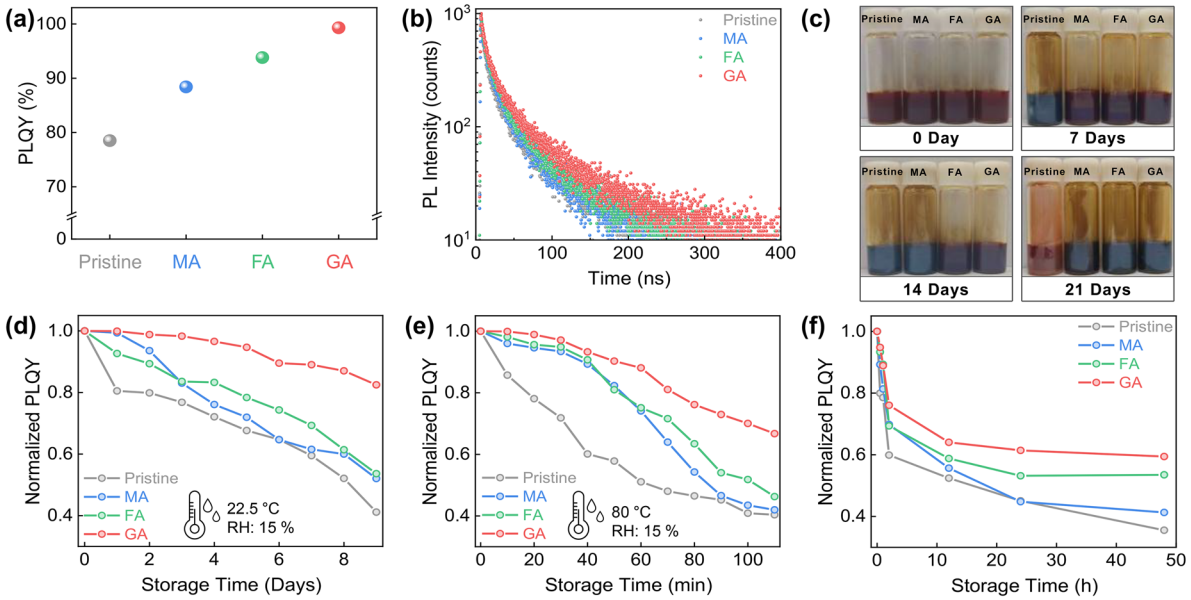

FIGURE 3 | Photophysical properties and stability characterization of pristine, MA-, FA-, and GA-treated PNCs. (a) PLQY values, (b) Time-resolved PL decay curves of each PNC sample. (c) Photographs of PNC dispersions stored under ambient conditions over time. (d) Time-dependent normalized PLQY of each PNC sample during storage at 22.5°C and 15% RH. (e) Normalized PLQY of each PNC sample under accelerated thermal stress at 80°C and 15% RH. (f) Normalized PLQY of each PNC sample under continuous 365 nm UV irradiation.

halides and ligands, thereby rigidifying the inorganic framework and stabilizing the $[PbI_6]^{4-}$ octahedral units [5, 47]. This interfacial anchoring suppresses the formation of defect states, including undercoordinated Pb^{2+} sites and halide vacancies. These combined characteristics indicate that GA provides the most comprehensive surface-regulation pathway among the tested modulators, integrating favorable incorporation energetics, efficient vacancy occupation, possible cation-exchange-assisted incorporation, and multiple hydrogen-bonding interactions [5, 48]. GA is most effective in suppressing trap formation and ion migration, resulting in superior surface stabilization compared with MA and FA.

2.3 | Photophysical Properties and Stability of Surface-Treated PNCs

The photophysical properties and stability of pristine, MA-, FA-, and GA-treated PNCs were systematically evaluated, as presented in Figure 3. The initial PLQY values of the PNC solutions were measured to be 78.5% (pristine), 88.4% (MA), 93.8% (FA), and 99.3% (GA) (Figure 3a). Notably, the GA-treated PNCs exhibited the highest PLQY, approaching unity, indicating that GA^+ is the most effective surface modulator among the three organic cations.

The impact of surface modulation on charge-carrier recombination dynamics was further investigated using the time-correlated single-photon counting (TCSPC) measurements (Figure 3b). The PL decay curves were fitted using a biexponential function to extract carrier lifetimes. The fast decay component (τ_1) is primarily attributed to trap-assisted non-radiative recombination, whereas the slow decay component (τ_2) is associated with radiative recombination [49]. The average carrier lifetime (τ_{avg}) increased systematically in the order of pristine (23.97 ns), MA (25.33 ns), FA (28.97 ns), and GA (33.19 ns) (Table S2), indicating progressively suppressed non-radiative recombination with improved surface passivation. Together with the XPS and FT-IR results, the prolonged carrier lifetime of GA-treated PNCs supports effective suppression of trap-assisted recombination.

To further quantify defect densities, space-charge-limited current (SCLC) measurements were performed using hole-only devices with a configuration of ITO/PEDOT:PSS/PNCs/MoO_3/Ag (Figure S25). The extracted trap-filled limit voltages (V_{TFL}) were 0.98 V (pristine), 0.91 V (MA), 0.86 V (FA), and 0.78 V (GA), showing a systematic decrease with improved surface modulation. The trap density (N_T) was calculated using Equation (1):

$$N_T = \frac{2\varepsilon_0 \varepsilon V_{TFL}}{eL^2} \quad (1)$$

where ε_0 is the vacuum permittivity (8.854×10^{-12} F m^{-1}), ε is the dielectric constant of $CsPbI_3$ (6.32), e is the elementary charge (1.6×10^{-19} C), and L is the thickness of the PNC film (~50 nm) [25, 50]. The calculated N_T values decreased from 2.74×10^{17} cm^{-3} (pristine) to 2.54×10^{17} cm^{-3} (MA), 2.40×10^{17} cm^{-3} (FA), and 2.18×10^{17} cm^{-3} (GA), in good agreement with the carrier lifetime trend and indicating progressive suppression of defect states.

The long-term stability of the surface-treated PNCs was further evaluated under multiple environmental stress conditions. The superior effect of GA modulation is visually evident from photographs of PNC dispersions stored under ambient conditions over time (Figure 3c), where the GA-treated sample maintains its original color, while the pristine sample undergoes a visible color change over the same period. The stability of the PNC dispersions was subsequently examined under ambient storage, accelerated thermal stress, continuous UV irradiation, and an

16136829, 2026, 64, Downloaded from https://onlinelibrary.wiley.com/doi/10.1002/smll.75614 by Hanyang University Library, Wiley Online Library on [22/11/2026]. See the Terms and Conditions (https://onlinelibrary.wiley.com/terms-and-conditions) on Wiley Online Library for rules of use; OA articles are governed by the applicable Creative Commons License

elevated-humidity condition (Figure 3d–f and Figure S29). Under ambient storage at 22.5°C and 15% RH, GA-treated PNCs maintained ~80% of their initial PLQY after 9 days, whereas the pristine sample declined to ~40% (Figure 3d and Figure S26). Under thermal stress at 80°C and 15% RH, GA-treated PNCs preserved ~70% of their initial PLQY after 100 min, while the pristine sample again fell to ~40% (Figure 3e). Under continuous UV irradiation (365 nm, 0.85 mW cm^{-2}), all treated PNCs exhibited higher photostability than the pristine sample. After 48 h of UV exposure, GA-treated PNCs retained ~59% of their initial PLQY, compared with ~36% for the pristine sample, whereas MA- and FA-treated PNCs retained ~41% and ~54%, respectively (Figure 3f). Under a more aggressive elevated-humidity condition at 22.5°C and 95% RH, GA-treated PNCs likewise retained a higher PLQY than the other samples, consistent with the visible color change observed for the stored PNC solutions (Figure S29 and S30). Under accelerated thermal, UV, and elevated-humidity stress conditions, the pristine PNCs exhibited a progressively more pronounced PL red-shift, whereas this spectral shift was increasingly suppressed upon MA-, FA-, and particularly GA-treatment (Figure S27, S28, and S31).

Taken together, these results indicate that the strong multidentate hydrogen-bonding interactions of GA^+ not only suppress non-radiative recombination but also enhance the resistance of the PNC surface to environmental degradation, leading to substantially improved stability under ambient, thermal, UV, and humid stress conditions.

2.4 | Optoelectronic Properties of Surface-Treated PNCs

To evaluate the device performance of the surface-treated PNCs, PeLEDs based on pristine, MA-, FA-, and GA-treated PNCs were fabricated with an n–i–p architecture (ITO/ZnMgO/PEIE/PNCs/TCTA/MoO_3/Al), as schematically illustrated in Figure 4a. The corresponding energy-level diagram and cross-sectional SEM image (Figure 4b,c) indicate suitable energy-level alignment and a well-defined multilayer device structure.

The current density-voltage (*J-V*), luminance-voltage (*L-V*), and EQE–voltage (*EQE-V*) characteristics of the fabricated PeLEDs are presented in Figure 4d–f. Among the devices, the GA-treated device achieved a maximum luminance of 473 cd m^{-2} and a maximum EQE of 10.2%, representing a significant improvement over the pristine device, which exhibited a maximum luminance of 231 cd m^{-2} and a maximum EQE of 7.2%. The MA- and FA-treated devices showed intermediate performance, with maximum EQEs of 7.7% and 9.4%, respectively (Table S3). The normalized electroluminescence (EL) spectra of all devices (Figure 4g and Figure S32) exhibited an emission peak centered at 687 nm with negligible spectral shifts, confirming that surface modulation does not alter the intrinsic emission characteristics of the PNCs. Operational lifetime measurements were conducted at an initial luminance of ~50 cd m^{-2} (Figure 4h). The T_{50} operational lifetimes were 1.17 min (pristine), 1.98 min (MA), 4.55 min (FA), and 5.72 min (GA). The GA-treated device exhibited the longest operational lifetime, corresponding to a 4.89-fold improvement over the pristine device. Furthermore, the surface temperature of the operating devices was recorded using an infrared camera under a constant current density of 72.6 mA cm^{-2} (Figure 4i). The surface temperature of the pristine device increased rapidly during device operation, reaching a maximum of 29.1°C at 2 min and subsequently decreasing to 28.7°C at 3 min. The MA-treated device also showed a comparable temperature increase, reaching 28.3°C at 3 min. In contrast, the FA- and GA-treated devices exhibited substantially smaller temperature increases, reaching 24.9°C and 24.1°C at 3 min, respectively. Since all devices were operated at the same current density, this reduced temperature rise of the treated devices is consistent with lower electrical power dissipation associated with their lower driving voltages, together with reduced non-radiative energy loss. Such Joule-heating-induced temperature increases during electrical operation are known to strongly influence the efficiency and operational stability of PeLEDs [51, 52].

To further examine ion-migration behavior at the device level, forward and reverse *J-V* scans were compared for the pristine, MA-, FA-, and GA-treated devices (Figure S33). The pristine and MA-treated devices exhibited noticeable hysteresis, consistent with field-driven ionic redistribution, whereas the hysteresis progressively diminished from the FA- to the GA-treated device, with the GA-treated device showing nearly overlapping forward and reverse curves. This suppression is consistent with the enhanced surface anchoring of the modulators and the increased iodine-vacancy formation energy (Figure S22–S24). Collectively, the extended operational lifetime, suppressed temperature rise, and diminished *J-V* hysteresis of the GA-treated device support the interpretation that the multidentate hydrogen bonding of GA^+ suppresses surface-halide migration and restricts the associated ionic redistribution underlying device degradation.

3 | Conclusions

In summary, MA, FA, and GA were systematically investigated as surface modulators for all-inorganic $CsPbI_3$ PNCs to clarify how molecular structure governs surface passivation. The results show that the passivation efficacy strongly depends on the strength and denticity of hydrogen-bonding interactions formed between the organic cations and the PNC surface. Among the three candidates, GA^+ was identified as the most effective modulator because its trifunctional structure provides multiple N—H hydrogen-bonding sites that enable robust multidentate interactions, thereby suppressing trap formation, non-radiative recombination, and halide ion migration. This molecular advantage translated directly into enhanced photophysical properties and environmental stability. GA-treated PNCs exhibited a near-unity PLQY of 99.3% and retained ~80% of their initial PLQY after 9 days under ambient conditions. When incorporated into PeLEDs, the corresponding devices delivered a maximum EQE of 10.2% and a peak luminance of 473 cd m^{-2}, together with markedly improved operational stability. Importantly, rather than simply identifying GA^+ as an effective passivating cation, this work establishes hydrogen-bonding denticity

16136829, 2026, 64, Downloaded from https://onlinelibrary.wiley.com/doi/10.1002/smll.75614 by Hanyang University Library, Wiley Online Library on [22/11/2026]. See the Terms and Conditions (https://onlinelibrary.wiley.com/terms-and-conditions) on Wiley Online Library for rules of use; OA articles are governed by the applicable Creative Commons License

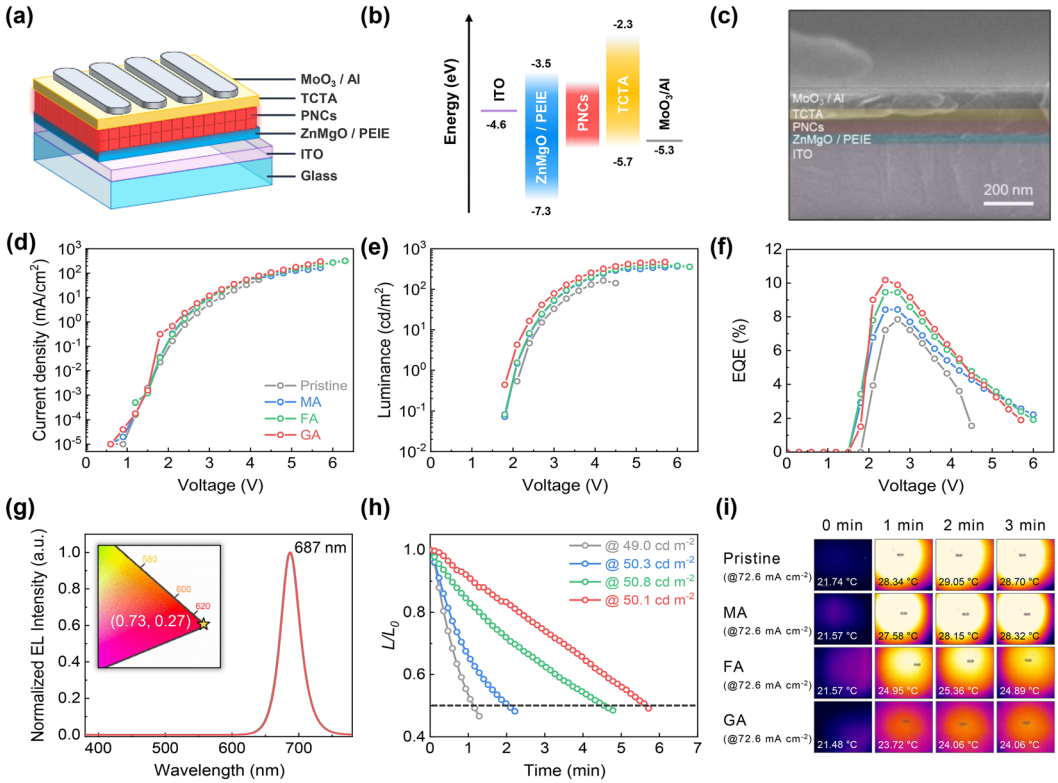

FIGURE 4 | Optoelectronic performance and device structure of PeLEDs based on pristine, MA-, FA-, and GA-treated PNCs. (a) Device architecture schematic, (b) Energy level diagram, (c) Cross-sectional SEM image of PeLED device. (d) *J-V*, (e) *L-V*, and (f) *EQE-V*. (g) Normalized EL spectra of each device at maximum EQE. (h) Operational stability curves measured under constant voltage. (i) Surface temperature profiles of operating devices under driving current of 72.6 mA cm^{-2}.

as a molecular descriptor for the distinct surface-modulation capabilities of structurally related MA^+, FA^+, and GA^+ cations. This comparative structure-mechanism framework provides a rational basis for the molecular design of surface modulators for efficient and stable PNC-based optoelectronic devices.

4 | Experimental Section

4.1 | Materials

Cesium carbonate (Cs_2CO_3, 99.9%), lead iodide (PbI_2; 99.999% trace metal basis), 1-octadecene (ODE; 90% tech.), oleylamine (OLA; 70% tech.), oleic acid (OAc; 90% tech.), ethyl acetate (EtOAc; anhydrous, 99.8%), polyethylenimine ethoxylated (PEIE; 37 wt.% in H_2O), toluene (anhydrous, 99.8%), n-hexane (anhydrous 95%), isopropanol (IPA; anhydrous 95%), ethanol (anhydrous 99.8%), acetone (anhydrous, 99.8%), dimethylsulfoxide (DMSO; anhydrous ≥ 99.9%), tetramethylammonium hydroxide pentahydrate (≥97%), zinc acetate dihydrate ($Zn(Ac)_2$; 99.9%), and magnesium acetate tetrahydrate ($Mg(Ac)_2$; 99.9%) were purchased from Sigma-Aldrich. Guanidinium iodide (GAI; 99.99%), methylammonium iodide (MAI; 99.99%), and formamidinium iodide (FAI; 99.99%) were purchased from Greatcell Solar. Molybdenum trioxide (MoO_3; 99.9995%) was purchased from Alfa Aesar. p-type 4,4′,4″-tris-(carbazol-9-yl) triphenylamine (TCTA) was purchased from Ossila. Aluminum (Al; 99.9%) and silver (Ag; 99.9%) were purchased from iTASCO.

4.2 | Synthesis of $CsPbI_3$ PNCs

To synthesize $CsPbI_3$ PNCs, two precursor solutions were prepared prior to synthesis. For the cesium oleate solution, Cs_2CO_3 (407 mg), 1.25 mL of OAc, and 20 mL of ODE were loaded into a three-neck round-bottom flask and degassed under vacuum at 100°C for 1 h. After degassing, the flask was filled with N_2 and the temperature was increased to 150°C and was maintained at this temperature for 30 min to ensure complete dissolution. For the PbI_2 precursor solution, PbI_2 (173 mg), 10 mL of ODE, 1 mL of OAc, and 1 mL of OLA were put into a 100 mL three-neck flask and degassed under vacuum at 100°C for 1 h. After degassing, the flask was filled with N_2, and the temperature was raised to 175°C. Upon reaching 175°C, 1 mL of the cesium oleate solution was rapidly injected. After 7 s, the flask was cooled in an ice bath.

4.3 | Purification of $CsPbI_3$ PNCs

For the first purification, the crude PNC dispersion was centrifuged at 7,000 rpm for 10 min. After discarding the supernatant, the resulting precipitate was redispersed in 2 mL of toluene. For the second purification step, 6 mL of EtOAc was added to 6.5 mL of the PNC dispersion, and the mixture was centrifuged at 10,000 rpm for 5 min. The supernatant was discarded, and the resulting pellet was redispersed in hexane. The solution was then centrifuged at 8,000 rpm for 3 min, and the supernatant was

16136829, 2026, 64, Downloaded from https://onlinelibrary.wiley.com/doi/10.1002/smll.75614 by Hanyang University Library, Wiley Online Library on [22/11/2026]. See the Terms and Conditions (https://onlinelibrary.wiley.com/terms-and-conditions) on Wiley Online Library for rules of use; OA articles are governed by the applicable Creative Commons License

filtered through a 0.2 μm PTFE membrane filter to obtain the final PNC solution.

4.4 | Anti-Solvent-Assisted Surface Modulation of $CsPbI_3$ PNCs

Following the first purification step, MAI, FAI, and GAI were dissolved separately in EtOAc with sonication at a concentration of 0.2 mg mL^{-1} (modulator solutions). For MA-, FA-, and GA-treated PNCs, 6 mL of each modulator solution was added to 6.5 mL of the PNC dispersion. The mixtures were centrifuged at 10 000 rpm for 5 min. The supernatants were discarded, and the resulting pellets were redispersed in hexane. The solutions were then centrifuged at 8,000 rpm for 3 min, and the supernatants were filtered through a 0.2 μm PTFE membrane filter to obtain the final PNC dispersions.

4.5 | Synthesis of ZnMgO NCs

$Zn(Ac)_2$ (2.7 mmol) and $Mg(Ac)_2$ (0.3 mmol) were dissolved in 30 mL of DMSO in a 100 mL three-neck flask. Under a N_2 atmosphere, the mixture was heated to boiling to ensure complete dissolution, maintained at reflux for 15 min, and then cooled to room temperature. After cooling, the reaction mixture was maintained at 30°C. Tetramethylammonium hydroxide pentahydrate (5.5 mmol) was dissolved in 10 mL of ethanol. Subsequently, the ethanol solution was added dropwise to the DMSO mixture, and the resulting solution was stirred at 30°C for 24 h. After that, ethyl acetate was added to precipitate ZnMgO, and the precipitate was redispersed in ethanol. This purification procedure was repeated twice. Finally, the solution was filtered through a 0.45 μm PTFE membrane filter and adjusted to a concentration of 7 mg mL^{-1} for subsequent use.

4.6 | LED Device Fabrication

ITO-coated glass substrates were sequentially cleaned by ultrasonication in deionized water, acetone, and IPA for 10 min each. After drying, the substrates were treated with O_2 plasma for 30 min. The ZnMgO NC solution (7 mg mL^{-1} in ethyl alcohol) was spin-coated onto the ITO substrate at 4000 rpm for 30 s and annealed at 150°C for 10 min. Subsequently, a PEIE solution dissolved in IPA (0.04 wt %) was spin-coated at 4000 rpm for 40 s and annealed at 110°C for 10 min. The $CsPbI_3$ PNC solution (35 mg mL^{-1} in hexane) was spin-coated at 3000 rpm for 30 s as the emissive layer. All spin-coating processes were carried out in an N_2-filled glovebox. After that, TCTA (50 nm), MoO_3 (8.5 nm), and Al (100 nm) were sequentially deposited at approximately 10^{-6} Torr using a thermal evaporator. The area of the Al electrode defined an emission area of 0.135 cm^2 of the device.

4.7 | Characterizations

Transmission electron microscopy (TEM) measurements were carried out using a JEM-2100F (JEOL). X-ray diffraction (XRD) patterns were obtained using X-ray diffractometer (Miniflex 600 B, Scitech Korea Inc.). Ultraviolet-visible (UV–vis) absorption was measured by a JASCO V-770. X-ray Photoelectron Spectroscopy (XPS) measurements were conducted using the NEXSA G2 (UVP, Inc.) analyzer. Fourier transform infrared (FT-IR) spectroscopy was performed using an IRTracer-100 (Shimadzu). The PL lifetimes were measured by time-correlated single-photon counting (TCSPC) using a DeltaPro fluorescence lifetime system (Horiba Scientific, FluoroMax Plus). A 375 nm picosecond pulsed laser diode was employed as the excitation source. PLQY was measured using Quantaurus-QY Absolute PLQY spectrometer (HAMAMATSU) with an excitation wavelength of 365 nm. Scanning Electron Microscope (SEM) images were obtained using a JSM-IT800 (JEOL). The surface temperature of operating devices was recorded using an infrared thermal imaging camera (PI 640i, Optris). For PeLED devices, *J-V*, *L-V*, *EQE-V*, and EL spectra characteristics were measured using a CS-2000 spectroradiometer (Konica Minolta) with a Keithley 2450 source meter in an N_2-filled glovebox.

4.8 | Density Functional Theory (DFT) Calculations

DFT calculations were performed to investigate the passivation characteristics of organic modulators using CASTEP program [53]. The generalized gradient approximation with Perdew-Burke-Ernzerhof functional was employed to correct the exchange-correlation energy [54]. Spin-polarized calculations were employed and van der Waals corrections were considered with Tkatchenko–Scheffler method [55]. Two-point steepest descents algorithm was employed [56]. The convergence criteria of energy, force, stress, displacement, and self-consistent field were set to 2×10^{-5} eV/atom, 0.05 eV/Å, 0.1 GPa, 2×10^{-3} Å, and 2×10^{-6} eV/atom, respectively. The energy cut-off value was set to 240 eV with ultrasoft pseudopotentials. $8 \times 8 \times 8$ *k*-points and *Γ*-point were used with Monkhorst-Pack grid for the cell optimization of α-$CsPbI_3$ unit cell and the surface systems, respectively [57]. The (100) surface of α-$CsPbI_3$ perovskite was considered for our DFT calculations, which was the dominant surface of α-$CsPbI_3$ perovskite structure.

Normalized incorporation energies were calculated by using the following Equation (2).

$$\text{Incorporation energy} = \frac{\left(E_{n\ \text{XAI incorporated}} + n \times E_{\text{CsI}}\right) - \left(n \times E_{\text{XAI}} + E_{\text{Pristine}}\right)}{n} \quad (2)$$

where $E_{n\ \text{XAI incorporated}}$, E_{CsI}, E_{XAI}, and E_{Pristine} are the energy of the $CsPbI_3$ surface incorporating n XAI molecules (n = 1, 2, and 3), the energy of the CsI molecule, the energy of the XAI molecule, and the energy of the pristine $CsPbI_3$ surface, respectively. Here, XAI denotes MAI, FAI, and GAI molecules.

16136829, 2026, 64, Downloaded from https://onlinelibrary.wiley.com/doi/10.1002/smll.75614 by Hanyang University Library, Wiley Online Library on [22/11/2026]. See the Terms and Conditions (https://onlinelibrary.wiley.com/terms-and-conditions) on Wiley Online Library for rules of use; OA articles are governed by the applicable Creative Commons License

Ratio of the Boltzmann distributions based on the normalized incorporation energies was calculated by using the following Equation (3).

$$\frac{P_{\text{1Top or 2Top}}}{P_{\text{1Sub,2Sub, or 1Top–1Sub}}} = \exp\left(\frac{E_{\text{1Sub,2Sub, or 1Top–1Sub}} - E_{\text{1Top or 2Top}}}{k_B \times T}\right) \quad (3)$$

where $P_{\text{1Top or 2Top}}$ and $P_{\text{1Sub, 2Sub or 1Top-1Sub}}$ are the relative probabilities of the state with Top configuration and state with Sub configuration, respectively. $E_{\text{1Top or 2Top}}$ and $E_{\text{1Sub, 2Sub or 1Top-1Sub}}$ are the normalized incorporation energies in the Top and Sub-containing configurations, respectively. For the MA and FA systems, the Top and Sub-containing configurations correspond to 1Top and 1Sub, respectively, whereas for the 2GA system, they correspond to 2Top and 2Sub or Top-Sub, respectively. k_B and T are the Boltzmann constant (8.617×10^{-5} eV/K) and the temperature of the system (298.15 K), respectively.

Binding energies were calculated by using the following Equation (4).

$$\text{Binding energy} = E_{\text{total}} - E_{n\ \text{CsI vacancies system}} - n \times E_{\text{XAI}} \quad (4)$$

where E_{total}, $E_{n\ \text{CsI vacancies system}}$, and E_{XAI} are the energy of the total system, the energy of the (100) surface of $CsPbI_3$ with n CsI vacancies ($n = 1$ for the 1MA and 1FA systems and $n = 2$ for the 2GA system), and the energy of the XAI molecule, respectively.

Defect formation energies were calculated by using the following Equation (5).

$$\text{Defect formation energy} = \left(E_{\text{I vacancy system}} + E_{\text{iodine atom}}\right) - E_{\text{total}} \quad (5)$$

where $E_{\text{I vacancy system}}$, $E_{\text{iodine atom}}$, and E_{total} are the energy of the pristine or two GA incorporated-$CsPbI_3$ surface with an iodine vacancy system, the energy of the iodine atom, and the energy of the total system, respectively.

Acknowledgements

This work was supported by National Research Foundation of Korea (NRF) grants funded by the Korea government (MSIT) (RS-2022-NR071756, RS-2025-00523067, RS-2026-25620461). This work was partly supported by a Korea Institute for Advancement of Technology (KIAT) grant funded by the Korea Government (MOTIE) (RS-2024-00418086, HRD Program for Industrial Innovation). This work was partly supported by the Korea Basic Science Institute (National Research Facilities and Equipment Center) funded by the Ministry of Education (RS-2025-02308784). This work was partly supported by the Technology Innovation Program Development Program funded by the Ministry of Trade, Industry & Energy (MOTIE) (RS-2023-00265858). It was also supported by the Samsung Research Funding & Incubation Center of Samsung Electronics under projects SRFC-MA2401-03. This research was supported by the International Science and Technology Cooperation Project under the Regional Science and Technology Innovation Plan of Hubei Province (No. 2025EHA013). This work was supported by the KRICT-SKKU bilateral Research Programs, Korea Research Institute of Chemical Technology & Sungkyunkwan University, 2024. This work was supported by "Global Value-Up 10X Project" grant funded by the GIST in 2026.

Conflicts of Interest

The authors declare no conflicts of interest.

Data Availability Statement

The data that support the findings of this study are available from the corresponding author upon reasonable request.

References

1. J. Shamsi, A. S. Urban, M. Imran, L. De Trizio, and L. Manna, "Metal Halide Perovskite Nanocrystals: Synthesis, Post-Synthesis Modifications, and Their Optical Properties," *Chemical Reviews* 119 (2019): 3296–3348, https://doi.org/10.1021/acs.chemrev.8b00644.

2. X. Shen, Y. Zhang, S. V. Kershaw, et al., "Zn-Alloyed $CsPbI_3$ Nanocrystals for Highly Efficient Perovskite Light-Emitting Devices," *Nano Letters* 19 (2019): 1552–1559, https://doi.org/10.1021/acs.nanolett.8b04339.

3. Y. Hassan, J. H. Park, M. L. Crawford, et al., "Ligand-Engineered Bandgap Stability in Mixed-halide Perovskite LEDs," *Nature* 591 (2021): 72–77, https://doi.org/10.1038/s41586-021-03217-8.

4. A.-Y. Lee, J. Kim, D. Lee, and M. H. Song, "Efficient and Stable Perovskite Nanocrystal Light-Emitting Diodes With Sulfobetaine-Based Ligand Treatment," *ACS Applied Electronic Materials* 5 (2023): 5325–5331, https://doi.org/10.1021/acsaelm.2c01781.

5. Z. Yu, X. Shen, X. Fan, et al., "Hydrogen Bond-Assisted Dual Passivation for Blue Perovskite Light-Emitting Diodes," *ACS Energy Letters* 8 (2023): 4296–4303, https://doi.org/10.1021/acsenergylett.3c01323.

6. S. Singh, A. Sen, S. L. Aneesha, et al., "Defect Passivation Strategies in Halide Perovskite Solar Cells and LEDs," *ACS Energy Letters* 11 (2026): 3060–3120, https://doi.org/10.1021/acsenergylett.5c04238.

7. X. Shen, K. Kang, Z. Yu, et al., "Passivation Strategies for Mitigating Defect Challenges in Halide Perovskite Light-Emitting Diodes," *Joule* 7 (2023): 272–308, https://doi.org/10.1016/j.joule.2023.01.008.

8. J. Kim, E. D. Jung, J. You, et al., "Perovskites for Next-Generation Colour Conversion Displays," *Nature Electronics* 8 (2025): 886–894, https://doi.org/10.1038/s41928-025-01456-5.

9. I. Mosquera-Lois, Y.-T. Huang, H. Lohan, J. Ye, A. Walsh, and R. L. Z. Hoye, "Multifaceted Nature of Defect Tolerance in Halide Perovskites and Emerging Semiconductors," *Nature Reviews Chemistry* 9 (2025): 287–304, https://doi.org/10.1038/s41570-025-00702-w.

10. L. Protesescu, S. Yakunin, M. I. Bodnarchuk, et al., "X = Cl, Br, and I): Novel Optoelectronic Materials Showing Bright Emission With Wide Color Gamut," *Nano Letters* 15 (2015): 3692–3696, https://doi.org/10.1021/nl5048779.

11. X. Mei, D. Jia, J. Chen, S. Zheng, and X. Zhang, "Approaching High-Performance Light-Emitting Devices Upon Perovskite Quantum Dots: Advances and Prospects," *Nano Today* 43 (2022): 101449, https://doi.org/10.1016/j.nantod.2022.101449.

12. H. Im, J.-O. Oh, Y. Lee, et al., "Heterogeneous Integration of Complementary Field-Effect Transistors for High-Performance Micro LED Displays," *Advanced Materials* 37 (2025): 2408034, https://doi.org/10.1002/adma.202408034.

13. H.-J. Seok, S. H. Kim, K. M. Yeom, J. H. Noh, and H.-K. Kim, "Cost-Effective Transparent N-Doped Tin Oxide Electrodes With Excellent Thermal and Chemical Stabilities Enabling Stable Perovskite Photovoltaics Based on Tin Oxide Electron Transport Layer," *Advanced Energy Materials* 14 (2024): 2303859, https://doi.org/10.1002/aenm.202303859.

14. N. Fiuza-Maneiro, J. Ye, W. H. Jeong, et al., "Delayed Halide-Rich Molecular Passivation of CsPbCl3 Perovskite Nanocrystals Enables Bright Violet Light-Emitting Diodes," *Angewandte Chemie International Edition* 65 (2026): 26012, https://doi.org/10.1002/anie.202526012.

15. J. Ye, C. Nicholls, W. H. Jeong, et al., "Stronger Lewis Base Antisolvents Improve Perovskite Nanocrystal Stability," *ACS Energy Letters* 11 (2026): 3993–4001, https://doi.org/10.1021/acsenergylett.6c00480.

16. V. C. Ho, Y. N. Thi, and T. H. Pham, "Functional Cellulose Interfacial Layer on Zinc Metal for Enhanced Reversibility in Aqueous Zinc Ion

16136829, 2026, 64, Downloaded from https://onlinelibrary.wiley.com/doi/10.1002/smll.75614 by Hanyang University Library, Wiley Online Library on [22/11/2026]. See the Terms and Conditions (https://onlinelibrary.wiley.com/terms-and-conditions) on Wiley Online Library for rules of use; OA articles are governed by the applicable Creative Commons License

Batteries," *Chemical Engineering Journal* 496 (2024): 153845, https://doi.org/10.1016/j.cej.2024.153845.

17. M. Son, Y. K. Kang, J. Kim, et al., "High-Performance Transparent p -Type Thin-Film Transistor and Circuit With Air-Stable CuI:Cd," *Advanced Functional Materials* 36 (2026): 20710, https://doi.org/10.1002/adfm.202520710.

18. J. Thiesbrummel, J. V. Milic, C. Deibel, et al., "Ion Migration in Perovskite Solar Cells," *Nature Reviews Chemistry* 10 (2026): 179–195, https://doi.org/10.1038/s41570-025-00790-8.

19. N. Li, Y. Jia, Y. Guo, et al., "Ion Migration in Perovskite Light-Emitting Diodes: Mechanism, Characterizations, and Material and Device Engineering," *Advanced Materials* 34 (2022): 2108102, https://doi.org/10.1002/adma.202108102.

20. E. M. Sanehira, A. R. Marshall, J. A. Christians, et al., "Quantum Dot Arrays for Record-Efficiency, High-Voltage Photovoltaic Cells," *Science Advances* 3 (2017): aao4204.

21. N. Quan, L. Ma, and D. Zhao, "Edge Stabilization in Reduced-Dimensional Perovskites," *Nature Communications* 11 (2020): 170, https://doi.org/10.1038/s41467-019-13944-2.

22. H. Li, H. Huang, D. Li, et al., "Buried Interface Engineering Enables Efficient and Refurbished $CsPbI_3$ Perovskite Quantum Dot Solar Cells," *Energy & Environmental Science* 18 (2025): 972–981, https://doi.org/10.1039/d4ee04628e.

23. W. H. Jeong, S. Lee, H. Song, et al., "Synergistic Surface Modification for High-Efficiency Perovskite Nanocrystal Light-Emitting Diodes: Divalent Metal Ion Doping and Halide-Based Ligand Passivation," *Advanced Science* 11 (2024): 2305383, https://doi.org/10.1002/advs.202305383.

24. W. H. Jeong, Z. Yu, L. Gregori, et al., "In Situ Cadmium Surface Passivation of Perovskite Nanocrystals for Blue LEDs," *Journal of Materials Chemistry A* 9 (2021): 26750–26757, https://doi.org/10.1039/d1ta08756h.

25. H. Song, J. Yang, W. H. Jeong, et al., "A Universal Perovskite Nanocrystal Ink for High-Performance Optoelectronic Devices," *Advanced Materials* 35 (2023): 2209486.

26. J. Uhm, Y. Byun, S. Park, S. Kim, and M.-J. Choi, "Iodide-Coated $CsPbBr_3$ Perovskite Nanowires for Resistive-Switching Memory in Neuromorphic Systems and Edge Computing," *Nano Letters* 26 (2026): 3503–3513, https://doi.org/10.1021/acs.nanolett.5c06511.

27. X. Zhang, H. Huang, C. Zhao, and J. Yuan, "Surface Chemistry-Engineered Perovskite Quantum Dot Photovoltaics," *Chemical Society Reviews* 54 (2025): 3017–3060, https://doi.org/10.1039/d4cs01107d.

28. Q. Feng and G. Nan, "How Do A-Site Cations Regulate Trap States at Defective Surfaces of Lead Iodide Perovskites?," *The Journal of Physical Chemistry Letters* 13 (2022): 4831–4839, https://doi.org/10.1021/acs.jpclett.2c01149.

29. Y.-H. Kim, S. Kim, A. Kakekhani, et al., "Comprehensive Defect Suppression in Perovskite Nanocrystals for High-Efficiency Light-Emitting Diodes," *Nature Photonics* 15 (2021): 148–155, https://doi.org/10.1038/s41566-020-00732-4.

30. H. Ebe, R. Suzuki, S. Sumikoshi, et al., "Guanidium Iodide Treatment of Size-Controlled $CsPbI_3$ Quantum Dots for Stable Crystal Phase and Highly Efficient Red LEDs," *Chemical Engineering Journal* 471 (2023): 144578, https://doi.org/10.1016/j.cej.2023.144578.

31. M. Ban, Y. Zou, J. P. H. Rivett, et al., "Solution-processed Perovskite Light Emitting Diodes With Efficiency Exceeding 15% Through Additive-controlled Nanostructure Tailoring," *Nature Communications* 9 (2018): 3892, https://doi.org/10.1038/s41467-018-06425-5.

32. C. Zhao, C. Cazorla, X. Zhang, et al., "Fast Organic Cation Exchange in Colloidal Perovskite Quantum Dots Toward Functional Optoelectronic Applications," *Journal of the American Chemical Society* 146 (2024): 4913–4921, https://doi.org/10.1021/jacs.3c14000.

33. M. T. Hoang, A. S. Pannu, Y. Yang, et al., "Surface Treatment of Inorganic CsPbI(3) Nanocrystals With Guanidinium Iodide for Efficient Perovskite Light-Emitting Diodes With High Brightness," *Nanomicro Letters* 14 (2022): 69, https://doi.org/10.1007/s40820-022-00813-9.

34. C. Guo, C. Bi, S. Wei, et al., "Highly Efficient and Stable $CsPbI_3$ Perovskite Quantum Dots Light-Emitting Diodes through Synergistic Effect of Halide-Rich Modulation and Lattice Repair," *Small* 21 (2025): 2409630.

35. J. Fu, J. Liu, L. Yuan, et al., "3D/2D Core/Shell Perovskite Nanocrystals for High-Performance Solar Cells," *Small* 19 (2023): 2207312.

36. D. Luo, R. Su, W. Zhang, et al., "Minimizing Non-Radiative Recombination Losses in Perovskite Solar Cells," *Nature Reviews Materials* 5 (2020): 44–60, https://doi.org/10.1038/s41578-019-0151-y.

37. T.-H. Han, S. Tan, J. Xue, L. Meng, J.-W. Lee, and Y. Yang, "Interface and Defect Engineering for Metal Halide Perovskite Optoelectronic Devices," *Advanced Materials* 31 (2019): 1803515, https://doi.org/10.1002/adma.201803515.

38. S. Han, G. Seo, T. Yong, et al., "Stabilized Perovskite Quantum Dot Solids via Nonpolar Solvent Dispersible Covalent Ligands," *Advanced Science (Weinh)* 10 (2023): 2301793, https://doi.org/10.1002/advs.202301793.

39. L. Protesescu, S. Yakunin, M. I. Bodnarchuk, et al., "Nanocrystals of Cesium Lead Halide Perovskites ($CsPbX_3$, X = Cl, Br, and I): Novel Optoelectronic Materials Showing Bright Emission With Wide Color Gamut," *Nano Letters* 15 (2015): 3692–3696, https://doi.org/10.1021/nl5048779.

40. J. Ye, Z. Li, D. J. Kubicki, et al., "Elucidating the Role of Antisolvents on the Surface Chemistry and Optoelectronic Properties of $CsPbBrxI_{3-x}$ Perovskite Nanocrystals," *Journal of the American Chemical Society* 144 (2022): 12102–12115, https://doi.org/10.1021/jacs.2c02631.

41. J. Ye, N. Mondal, B. P. Carwithen, et al., "Extending the Defect Tolerance of Halide Perovskite Nanocrystals to Hot Carrier Cooling Dynamics," *Nature Communications* 15 (2024): 8120, https://doi.org/10.1038/s41467-024-52377-4.

42. W. H. Jeong, J. Ye, J. Kim, et al., "Enhanced Stability and Linearly Polarized Emission From $CsPbI_3$ Perovskite Nanoplatelets Through A-site Cation Engineering," *Light: Science & Applications* 15 (2026): 22, https://doi.org/10.1038/s41377-025-02135-y.

43. Y. Fu, J. Xu, H. Han, et al., "Azetidinium Chloride-Assisted Early Crystallization and Defect Passivation via Wet-Film Treatment in $CsPbI_3$ Perovskite Solar Cells," *Small* 22 (2026): 08334.

44. C. Otero-Martínez, J. Ye, L. De Trizio, et al., "Organic A-Site Cations Improve the Resilience of Inorganic Lead-Halide Perovskite Nanocrystals to Surface Defect Formation," *Advanced Functional Materials* 34 (2024): 2404399, https://doi.org/10.1002/adfm.202404399.

45. J. Su, T. Hu, X. Chen, et al., "Multi-Functional Interface Passivation via Guanidinium Iodide Enables Efficient Perovskite Solar Cells," *Advanced Functional Materials* 34 (2024): 2406324.

46. Z. Ni, C. Bao, Y. Liu, et al., "Resolving Spatial and Energetic Distributions of Trap States in Metal Halide Perovskite Solar Cells," *Science* 367 (2020): 1352–1358, https://doi.org/10.1126/science.aba0893.

47. C. Greve, E. T. J. Nibbering, and H. Fidder, "Hydrogen-Bonding-Induced Enhancement of Fermi Resonances: A Linear IR and Nonlinear 2D-IR Study of Aniline-d5," *The Journal of Physical Chemistry B* 117 (2013): 15843–15855, https://doi.org/10.1021/jp4084103.

48. Z. Li, Z. Chen, Z. Shi, et al., "Charge Injection Engineering at Organic/Inorganic Heterointerfaces for High-Efficiency and Fast-Response Perovskite Light-Emitting Diodes," *Nature Communications* 14 (2023): 6441, https://doi.org/10.1038/s41467-023-41929-9.

49. Z. Yu, Y. Choi, X. Shen, et al., "Phosphonic Acid Based Bifunctional Additive for High-Performance Blue Perovskite Light-Emitting Diodes," *Nano Energy* 125 (2024): 109552, https://doi.org/10.1016/j.nanoen.2024.109552.

50. J. Kim, R. F. B. Nasrun, W. H. Jeong, et al., "Conjugated Polyelectrolytes as a Defect-Passivating Hole Injection Layer for Efficient and Stable Perovskite Light-Emitting Diodes," *ACS Applied Electronic Materials* 6 (2024): 8929–8937, https://doi.org/10.1021/acsaelm.4c01635.

16136829, 2026, 64, Downloaded from https://onlinelibrary.wiley.com/doi/10.1002/smll.75614 by Hanyang University Library, Wiley Online Library on [22/11/2026]. See the Terms and Conditions (https://onlinelibrary.wiley.com/terms-and-conditions) on Wiley Online Library for rules of use; OA articles are governed by the applicable Creative Commons License

51. X. Shen, S. L. Kwak, W. H. Jeong, et al., "Thermal Management Enables Stable Perovskite Nanocrystal Light-Emitting Diodes With Novel Hole Transport Material," *Small* 19 (2023): 2303472.

52. H. Xu, X. Wang, Y. Li, et al., "Prominent Heat Dissipation in Perovskite Light-Emitting Diodes With Reduced Efficiency Droop for Silicon-Based Display," *The Journal of Physical Chemistry Letters* 11 (2020): 3689–3698, https://doi.org/10.1021/acs.jpclett.0c00792.

53. S. J. Clark, M. D. Segall, C. J. Pickard, et al., "First Principles Methods Using CASTEP," *Zeitschrift für kristallographie* 220 (2005): 567–570.

54. J. P. Perdew, K. Burke, and M. Ernzerhof, "Generalized Gradient Approximation Made Simple," *Physical Review Letters* 77 (1996): 3865–3868, https://doi.org/10.1103/PhysRevLett.77.3865.

55. A. Tkatchenko and M. Scheffler, "Accurate Molecular Van Der Waals Interactions From Ground-State Electron Density and Free-Atom Reference Data," *Physical Review Letters* 102 (2009): 073005, https://doi.org/10.1103/PhysRevLett.102.073005.

56. J. Barzilai and J. M. Borwein, "Two-Point Step Size Gradient Methods," *IMA Journal of Numerical Analysis* 8 (1988): 141–148, https://doi.org/10.1093/imanum/8.1.141.

57. J. D. Pack and H. J. Monkhorst, ""Special Points for Brillouin-Zone Integrations"—a Reply," *Physical Review B* 16 (1977): 1748–1749, https://doi.org/10.1103/PhysRevB.16.1748.

Supporting Information

Additional supporting information can be found online in the Supporting Information section.

Supporting File: smll75614-sup-0001-SuppMat.docx.

16136829, 2026, 64, Downloaded from https://onlinelibrary.wiley.com/doi/10.1002/smll.75614 by Hanyang University Library, Wiley Online Library on [22/11/2026]. See the Terms and Conditions (https://onlinelibrary.wiley.com/terms-and-conditions) on Wiley Online Library for rules of use; OA articles are governed by the applicable Creative Commons License